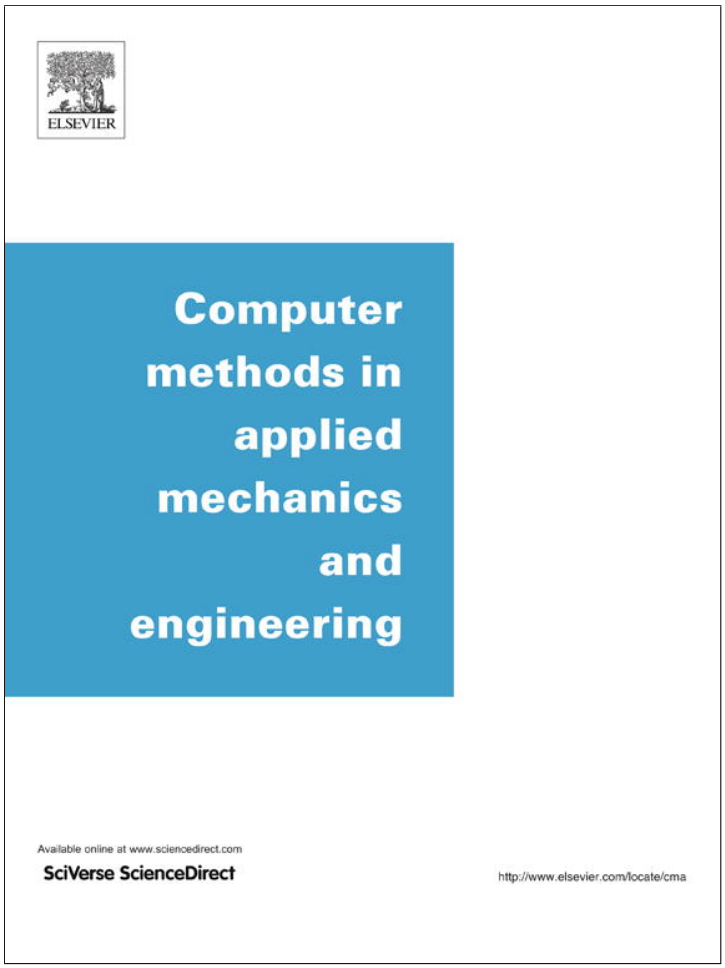

Comput. Methods Appl. Mech. Engrg. 261-262 (2013) 105–117

Contents lists available at SciVerse ScienceDirect

Comput. Methods Appl. Mech. Engrg.

journal homepage: www.elsevier.com/locate/cma

# A Finite element discretization of the streamfunction formulation of the stationary quasi-geostrophic equations of the ocean

Erich L Foster [a], Traian Iliescu [a,*], Zhu Wang [b]

[a] Department of Mathematics, Virginia Tech, Blacksburg, VA 24061-0123, USA
[b] Institute for Mathematics and its Applications, University of Minnesota, Minneapolis, MN 55455-0134, USA

ARTICLE INFO

*Article history:*
Received 8 December 2012
Received in revised form 19 April 2013
Accepted 23 April 2013
Available online 30 April 2013

*Keywords:*
Quasi-geostrophic equations
Finite element method
Argyris element

ABSTRACT

This paper presents a conforming finite element discretization of the streamfunction formulation of the one-layer stationary quasi-geostrophic equations, which are a commonly used model for the large scale wind-driven ocean circulation. Optimal error estimates for this finite element discretization with the Argyris element are derived. To the best of the authors' knowledge, these represent the first optimal error estimates for the finite element discretization of the quasi-geostrophic equations. Numerical tests for the finite element discretization of the quasi-geostrophic equations and two of its standard simplifications (the linear Stommel model and the linear Stommel–Munk model) are carried out. By benchmarking the numerical results against those in the published literature, we conclude that our finite element discretization is accurate. Furthermore, the numerical results have the same convergence rates as those predicted by the theoretical error estimates.



## 1. Introduction

With the continuous increase in computational power, complex mathematical models are becoming more and more popular in the numerical simulation of oceanic and atmospheric flows. For some geophysical flows in which computational efficiency is of paramount importance, however, simplified mathematical models are central. For example, the *quasi-geostrophic equations (QGE)*, a standard mathematical model for large scale oceanic and atmospheric flows [1–4], are often used in climate modeling [5].

The QGE are usually discretized in space by using the *finite difference method (FDM)* (see, e.g., [6]) or by the *finite volume method (FVM)* (see, e.g., [7,8]). The FVM is particularly appealing for geophysical flows since it can be used on unstructured grids and can preserve the conservation properties of the underlying equations. The *finite element method* (FEM), however, offers several advantages over the popular FDM, as outlined in [9]: (i) an easy treatment of complex boundaries, such as those of continents for the ocean, or mountains for the atmosphere; (ii) an easy grid refinement to achieve a high resolution in regions of interest [10]; (iii) a natural treatment of boundary conditions; and (iv) a straightforward approach for the treatment of multiply connected domains [9]. Despite these advantages, there are relatively few papers that consider the FEM applied to the QGE. Most *finite element (FE)* discretizations of the QGE have been developed for the streamfunction–vorticity formulation (see, e.g., [9–18]), very few using the streamfunction formulation (see, e.g., [12]). The reason is simple: The streamfunction–vorticity formulation yields a second order *partial differential equation (PDE)*, whereas the streamfunction formulation yields a fourth order PDE. Thus, although the streamfunction–vorticity formulation has two variables ($q$ and $\psi$) and the streamfunction formulation has just one ($\psi$), the former is the preferred formulation used in practical computations, since its conforming FE discretization requires low-order ($C^0$) elements, whereas the latter requires high-order ($C^1$) elements (see, e.g., Section 11.3 and Section 13.1 in [19] for the *Navier–Stokes equation (NSE)* setting). Thus, the state-of-the-art in the FE discretization of the QGE seems to reflect that for the 2D NSE, to which the QGE are similar in form. Indeed, most FE discretizations for the 2D NSE have used the streamfunction–vorticity formulation and $C^0$ elements, and relatively few have used the streamfunction formulation and $C^1$ elements (see [19–21] for a detailed presentation of both approaches). We note, however, that the streamfunction formulation of the 2D NSE and its discretization by $C^1$ elements is an active area of research (see, e.g., [22–32]).

Although the FE discretizations of the QGE are relatively scarce, the corresponding error analysis seems to be even more scarce. To our knowledge, *all* the error analysis for the FE discretization of the QGE has been done for the streamfunction–vorticity formulation, and none has been done for the streamfunction formulation.

* Corresponding author.
*E-mail addresses:* erichlf@vt.edu (E.L Foster), iliescu@vt.edu (T. Iliescu), wangzhu@ima.umn.edu (Z. Wang).
*URLs:* http://www.math.vt.edu/people/erichlf (E.L Foster), http://www.math.vt.edu/people/iliescu (T. Iliescu), http://www.ima.umn.edu/~wangzhu (Z. Wang).

0045-7825/$ - see front matter © 2013 Elsevier B.V. All rights reserved.
http://dx.doi.org/10.1016/j.cma.2013.04.008

Furthermore, to the best of our knowledge, all the available error estimates for the FE discretization of the QGE are *suboptimal*. The first error analysis for the FE discretization of the QGE was carried out by Fix [11], in which suboptimal error estimates for the streamfunction–vorticity formulation were proved. Indeed, relationships (4.7) and (4.8) (and the discussion above these) in [11] show that the FE approximations for *both* the potential vorticity (denoted by $\zeta$) and streamfunction (denoted by $\psi$) consist of piecewise polynomials of degree $k-1$. At the top of page 381, the author concludes that the error analysis yields the following estimates:

$$\|\psi-\psi^h\|_1 = O(h^{k-1}), \tag{1}$$

$$\|\zeta-\zeta^h\|_0 = O(h^{k-1}), \tag{2}$$

where $\|\cdot\|_0$ and $\|\cdot\|_1$ denote the $L^2$ and the $H^1$ norms, respectively. Although the streamfunction error estimate (1) appears to be optimal, the potential vorticity error estimate (2) is clearly suboptimal. Indeed, using piecewise polynomials of degree $k-1$ for the FE approximation of the vorticity, one would expect an $O(h^k)$ error estimate in the $L^2$ norm. Medjo [14,15] used a FE discretization of the streamfunction–vorticity formulation and proved error estimates for the time discretization, but no error estimates for the spatial discretization. Finally, Cascon et al. [10] proved both *a priori* and *a posteriori* error estimates for the FE discretization of the *linear Stommel–Munk* model (see Section 5.2 for more details). This model, while similar to the QGE, has one significant difference: the linear Stommel–Munk model is linear, whereas the QGE are nonlinear.

We note that the state-of-the-art in the FE error analysis for the QGE seems to reflect that for the 2D NSE. Indeed, as carefully discussed in [19] (see also [33–36]), the 2D NSE in streamfunction–vorticity formulation are easy to implement (only $C^0$ elements are needed for a conforming discretization), but the available error estimates are suboptimal (see Section 11.6 in [19]). Next, we summarize the discussion in [19], since we believe it sheds light on the QGE setting. For $C^0$ piecewise polynomial of degree $k$ FE approximation for *both* the vorticity (denoted by $\omega$) and streamfunction (denoted by $\psi$), the error estimates given in [21] are (see (11.26) in [19]):

$$|\psi-\psi^h|_1 + \|\omega-\omega^h\|_0 \leqslant C h^{k-1/2}\,|\ln h|^{\sigma}, \tag{3}$$

where $|\cdot|_1$ denotes the $H^1$ seminorm, $\sigma=1$ for $k=1$ and $\sigma=0$ for $k>1$. It is noted in [19] that the error estimate in (3) is not optimal: one may loose a half power in $h$ for the derivatives of the streamfunction (i.e., for the velocity), and three-halves power for the vorticity. It is also noted that there is computational and theoretical evidence that (3) is not sharp with respect to the streamfunction error. Furthermore, in [37] it was shown that, for the *linear* Stokes equations, the derivatives of the streamfunction are essentially optimally approximated (see (11.27) in [19]):

$$|\psi-\psi^h|_1 \leqslant C h^{k-\varepsilon}, \tag{4}$$

where $\varepsilon=0$ for $k>1$ and $\varepsilon>0$ is arbitrary for $k=1$. It is, however, noted in [19] that (3) seems to be sharp for the vorticity error and thus vorticity approximations are generally poor.

The FE discretization of the streamfunction formulation generally requires the use of $C^1$ elements (for a conforming discretization), which makes their implementation challenging. From a mathematical point of view, however, the streamfunction formulation is appealing, since there are optimal error estimates for the FE discretization of the streamfunction formulation (see the error estimate (13.5) and Table 13.1 in [19]).

The main goal of this paper is twofold. First, we use a $C^1$ finite element (the Argyris element) to discretize the streamfunction formulation of the QGE. To the best of our knowledge, this is the *first* time that a $C^1$ finite element has been used in the numerical discretization of the QGE. Second, we derive optimal error estimates for the FE discretization of the QGE and present supporting numerical experiments. To the best of our knowledge, this is the *first* time that optimal error estimates for the QGE have been derived.

The rest of the paper is organized as follows: Section 2 presents the QGE, their weak formulation, and mathematical support for the weak formulation. Section 3 outlines the FE discretization of the QGE, posing a special emphasis of the Argyris element. Rigorous error estimates for the FE discretization of the stationary QGE are derived in Section 4. Several numerical experiments supporting the theoretical results are presented in Section 5. Finally, conclusions and our future research directions are included in Section 6.

## 2. The quasi-geostrophic equations

The large scale ocean flows, which play a significant role in climate dynamics [5,38], are driven by two major sources: the wind and the buoyancy (see, e.g., Chapters 14–16 in [4]). Winds drive the subtropical and subpolar gyres, which correspond to the strong, persistent, subtropical and subpolar western boundary currents in the North Atlantic Ocean (the Gulf Stream and the Labrador Current) and North Pacific Ocean (the Kuroshio and the Oyashio Currents), as well as their subtropical counterparts in the southern hemisphere [5,4]. One of the common features of these gyres is that they display strong western boundary currents, weak interior flows, and weak eastern boundary currents.

One of the most popular mathematical models used in the study of large scale wind-driven ocean circulation is the QGE [1,4]. The QGE represent a simplified model of the full-fledged equations (e.g., the Boussinesq equations), which allows efficient numerical simulations while preserving many of the essential features of the underlying large scale ocean flows. The assumptions used in the derivation of the QGE include the hydrostatic balance, the $\beta$-plane approximation, the geostrophic balance, and the eddy viscosity parametrization. Details of the derivation of the QGE and the approximations used along the way can be found in standard textbooks on geophysical fluid dynamics, such as [1,39,2,40,3,4].

In the *one-layer QGE*, sometimes called the barotropic vorticity equation, the flow is assumed to be homogenous in the vertical direction. Thus, stratification effects are ignored in this model. The practical advantages of such a choice are obvious: the computations are two-dimensional, and, thus, the corresponding numerical simulation have a low computational cost. To include stratification effects, QGE models of increasing complexity have been devised (e.g., the two-layer QGE, the $N$-layer QGE, and the continuously stratified QGE [4]). As a first step, in this report we use the one-layer QGE (referred to as "the QGE" in what follows) to study the wind-driven circulation in an enclosed, midlatitude rectangular basin, which is a standard problem, studied extensively by ocean modelers [1,39,2,40,3,4].

The nondimensional *streamfunction–vorticity formulation* of the *stationary one-layer quasi-geostrophic equations* is (see, e.g., Eq. (14.57) in [4], Eq. (1.1) in [2], Eq. (1.1) in [41], and Eq. (1) in [42]):

$$J(\psi,q) = -Re^{-1}\,\Delta q + F \tag{5}$$

$$q = -Ro\,\Delta\psi + y, \tag{6}$$

where $\psi$ is the velocity streamfunction, $q$ is the potential vorticity, $F$ is the forcing, $J(\cdot,\cdot)$ is the Jacobian operator given by

$$J(\psi,q) := \frac{\partial\psi}{\partial x}\frac{\partial q}{\partial y} - \frac{\partial\psi}{\partial y}\frac{\partial q}{\partial x}, \tag{7}$$

$Re$ is the Reynolds number, and $Ro$ is the Rossby number. The Rossby number, $Ro$, is defined as (see, e.g., [42,43])

$$Ro := \frac{U}{\beta L^2}, \tag{8}$$

where $\beta$ is the coefficient multiplying the $y$ coordinate in the $\beta$-plane approximation [1,4], $L$ is the width of the computational domain, and $U$ is the Sverdrup velocity obtained from the balance between the $\beta$-effect and the curl of the divergence of the wind stress [4]. The Reynolds number, $Re$, is defined as

$$Re := \frac{UL}{A}, \tag{9}$$

where $A$ is the eddy viscosity parametrization. The horizontal velocity $\mathbf{u}$ can be recovered from $\psi$ by using the following formula: $\mathbf{u} = \left(\frac{\partial\psi}{\partial y}, -\frac{\partial\psi}{\partial x}\right)$.

Substituting (6) in (5) and dividing by $Ro$, we get the *streamfunction formulation* of the *stationary one-layer quasi-geostrophic equations*

$$Re^{-1}\,\Delta^2\psi + J(\psi, \Delta\psi) - Ro^{-1}\,\frac{\partial\psi}{\partial x} = Ro^{-1}\,F. \tag{10}$$

We note that the streamfunction–vorticity formulation has two unknowns ($q$ and $\psi$), whereas the streamfunction formulation has only one unknown ($\psi$). Because the streamfunction–vorticity formulation is a second-order PDE, whereas the streamfunction formulation is a fourth-order PDE, the former is more popular in practical computations.

We also note that (5)–(6) and (10) are similar in form to the 2D NSE written in the streamfunction–vorticity and streamfunction formulations, respectively. There are, however, several significant differences between the QGE and the 2D NSE. First, the term $y$ in (6) and the corresponding term $\frac{\partial\psi}{\partial x}$ in (10), which model the *rotation effects* in the QGE, do not have counterparts in the 2D NSE. Second, the Rossby number, $Ro$, in the QGE, which is a measure of the rotation effects, does not appear in the 2D NSE.

Next, we comment on the significance of the two parameters in (10), the Reynolds number, $Re$, and the Rossby number, $Ro$. As in the 2D NSE case, $Re$ is the coefficient of the diffusion term $-\Delta q = \Delta^2\psi$. The higher the Reynolds number $Re$, the smaller the magnitude of the diffusion term as compared with the nonlinear convective term $J(\psi, \Delta\psi)$. For small $Ro$, which corresponds to large rotation effects, the forcing term, $Ro^{-1}F$, becomes large compared with the other terms. The term $Ro^{-1}\,\frac{\partial\psi}{\partial x}$ could be interpreted as a convection type term with respect to $\psi$, not to $q = -\Delta\psi$. When $Ro$ is small, $Ro^{-1}\,\frac{\partial\psi}{\partial x}$ becomes large. Thus, the physically relevant cases for large scale oceanic flows, in which $Re$ is large and $Ro$ is small (i.e., small diffusion and high rotation, respectively) translate mathematically into a *convection-dominated* PDE with *large forcing*. Thus, from a mathematical point of view, we expect the restrictive conditions used to prove the well-posedness of the 2D NSE [20,21,19] to be even more restrictive in the QGE setting, due to the rotation effects. We will later see that this is indeed the case.

To completely specify the equations in (10), we need to impose boundary conditions. The question of appropriate boundary conditions for the QGE is a thorny one, especially for the streamfunction–vorticity formulation (see, e.g., [44,4]). In this report, we consider $\psi = \frac{\partial\psi}{\partial\mathbf{n}} = 0$ on $\partial\Omega$, which are also used in [19] for the streamfunction formulation of the 2D NSE.

To derive the weak formulation of the QGE (10), we first introduce the appropriate functional setting. Let $X := H_0^2(\Omega) = \left\{\psi \in H^2(\Omega) : \psi = \frac{\partial\psi}{\partial\mathbf{n}} = 0 \text{ on } \partial\Omega\right\}$. Multiplying (10) by a test function $\chi \in X$ and using the divergence theorem, we get the *weak formulation* of the QGE in streamfunction formulation [19]:

$$Re^{-1}\int_\Omega \Delta\psi\,\Delta\chi\,d\mathbf{x} + \int_\Omega \Delta\psi\left(\psi_y\,\chi_x - \psi_x\,\chi_y\right)d\mathbf{x} - Ro^{-1}\int_\Omega \psi_x\,\chi\,d\mathbf{x} = Ro^{-1}\int_\Omega F\,\chi\,d\mathbf{x} \quad \forall\,\chi \in X. \tag{11}$$

Therefore, letting

$$a_0(\psi,\chi) = Re^{-1}\int_\Omega \Delta\psi\,\Delta\chi\,d\mathbf{x}, \tag{12}$$

$$a_1(\zeta,\psi,\chi) = \int_\Omega \Delta\zeta\left(\psi_y\,\chi_x - \psi_x\,\chi_y\right)d\mathbf{x}, \tag{13}$$

$$a_2(\psi,\chi) = -Ro^{-1}\int_\Omega \psi_x\,\chi\,d\mathbf{x}, \tag{14}$$

$$\ell(\chi) = Ro^{-1}\int_\Omega F\,\chi\,d\mathbf{x} \tag{15}$$

gives the weak formulation of the QGE in streamfunction formulation: Find $\psi \in X$ such that

$$a_0(\psi,\chi) + a_1(\psi,\psi,\chi) + a_2(\psi,\chi) = \ell(\chi), \quad \forall\chi \in X. \tag{16}$$

The linear form $\ell$, the bilinear forms $a_0$ and $a_2$, and the trilinear form $a_1$ are continuous: There exist $\Gamma_1 > 0$ and $\Gamma_2 > 0$ such that

$$|a_0(\psi,\chi)| \leqslant Re^{-1}\,|\psi|_2\,|\chi|_2 \quad \forall\psi,\chi \in X, \tag{17}$$

$$|a_1(\zeta,\psi,\chi)| \leqslant \Gamma_1\,|\zeta|_2\,|\psi|_2\,|\chi|_2 \quad \forall\zeta,\psi,\chi \in X, \tag{18}$$

$$|a_2(\psi,\chi)| \leqslant Ro^{-1}\,\Gamma_2\,|\psi|_2\,|\chi|_2 \quad \forall\psi,\chi \in X, \tag{19}$$

$$|\ell(\chi)| \leqslant Ro^{-1}\,\|F\|_{-2}\,|\chi|_2 \quad \forall\chi \in X. \tag{20}$$

Inequalities (17), (18), and (20) are stated in [45] (see inequalities (2.2) and (2.3) in [45]). Inequality (19) can be proved as follows. Proposition 2.1 (iii) in [14] implies that

$$|a_2(\psi,\chi)| \leqslant Ro^{-1}\,C\,\|\psi\|_2\,\|\chi\|_2, \tag{21}$$

where $C$ is a generic constant. Theorem 1.1 in [21] implies that $|\cdot|_2$, the $H^2$ seminorm, and $\|\cdot\|_2$, the $H^2$ norm are equivalent on $X = H_0^2$. Thus, (21) yields inequality (19).

For small enough data, one can use the same type of arguments as those in Chapter 6 in [46] (see also [20,21]) to prove that the steady QGE in streamfunction formulation (16) are well-posed [47,48]. In what follows, we will always assume that the small data condition involving $Re, Ro$ and $F$, is satisfied and, thus, that there exists a unique solution $\psi$ to (16).

Using a standard argument [45], one can also prove the following stability estimate:

**Theorem 1.** *The solution $\psi$ of (16)satisfies the following stability estimate*:

$$|\psi|_2 \leqslant Re\,Ro^{-1}\,\|F\|_{-2}. \tag{22}$$

**Proof.** Setting $\chi = \psi$ in (16), we get:

$$a_0(\psi,\psi) + a_1(\psi,\psi,\psi) + a_2(\psi,\psi) = \ell(\psi). \tag{23}$$

Since the trilinear form $a_1$ is skew-symmetric in the last two arguments [20,21,19], we have

$$a_1(\psi,\psi,\psi) = 0. \tag{24}$$

We also note that, applying Green's theorem, we have

$$\begin{aligned} a_2(\psi,\psi) &= -Ro^{-1}\int\int_\Omega \frac{\partial\psi}{\partial x}\,\psi\,dx\,dy = -\frac{Ro^{-1}}{2}\int\int_\Omega \frac{\partial}{\partial x}(\psi^2)\,dx\,dy \\ &= -\frac{Ro^{-1}}{2}\int\int_\Omega \left(\frac{\partial}{\partial x}(\psi^2) - \frac{\partial}{\partial y}(0)\right)dx\,dy \\ &= -\frac{Ro^{-1}}{2}\int_{\partial\Omega} 0\,dx + \psi^2\,dy = 0, \end{aligned} \tag{25}$$

where in the last equality in (25) we used that $\psi = 0$ on $\partial\Omega$ (since $\psi \in H_0^2(\Omega)$). Substituting (25) and (24) in (23) and using the Cauchy–Schwarz inequality, we get:

$$|\psi|_2^2 = \int_\Omega \Delta\psi\,\Delta\psi\,d\mathbf{x} = Re\,Ro^{-1}\int_\Omega F\,\psi\,d\mathbf{x} \leqslant Re\,Ro^{-1}\,\|F\|_{-2}\,|\psi|_2, \tag{26}$$

which proves (22). □

## 3. Finite element formulation

In this section, we present the functional setting and some auxiliary results for the FE discretization of the streamfunction formulation of the QGE (16). Let $\mathcal{T}^h$ denote a finite element triangulation of $\Omega$ with meshsize (maximum triangle diameter) $h$. We consider a *conforming* FE discretization of (16), i.e., $X^h \subset X = H_0^2(\Omega)$.

The FE discretization of the streamfunction formulation of the QGE (16) reads: Find $\psi^h \in X^h$ such that

$$a_0(\psi^h,\chi^h) + a_1(\psi^h,\psi^h,\chi^h) + a_2(\psi^h,\chi^h) = \ell(\chi^h), \quad \forall\,\chi^h \in X^h. \tag{27}$$

Using standard arguments [20,21], one can prove that, if the small data condition used in proving the well-posedness result for the continuous case holds, then (27) has a unique solution $\psi^h$ (see Theorem 2.1 and subsequent discussion in [45]). One can also prove the following stability result for $\psi^h$ using the same arguments as those used in the proof of Theorem 1 for the continuous setting.

**Theorem 2.** *The solution $\psi^h$ of (27) satisfies the following stability estimate:*

$$|\psi^h|_2 \leqslant Re\,Ro^{-1}\,\|F\|_{-2}. \tag{28}$$

**Remark 1.** Note that Eq. (24), which was proven in the continuous case, also holds in the discrete case:

$$a_1(\psi^h,\psi^h,\psi^h) = 0 \quad \forall\,\psi^h \in X^h. \tag{29}$$

We emphasize that (29) holds because the trilinear form $a_1(\cdot,\cdot,\cdot)$ defined in (13) has been explicitly skew-symmetrized. Thus, no extra care needs to be taken to enforce (29) in our QGE setting; this is in clear contrast with the NSE setting, where special care is needed to enforce (29) (see, e.g., [49]). We also note that Eq. (25) holds in the discrete case as well:

$$a_2(\psi^h,\psi^h) = 0 \quad \forall\,\psi^h \in X^h. \tag{30}$$

**Remark 2.** The conservation properties of the FE discretization of the QGE have been proved in the pioneering paper of Fix [11]. In that report, it was shown that the FE discretization of the streamfunction–vorticity formulation of the QGE preserves the conservation properties of the continuum system: conservation of potential vorticity (equation (5.1) in [11]), conservation of potential enstrophy (equation (5.2) in [11]), and conservation of kinetic energy (equation (5.3) in [11]). Since only the streamfunction is explicitly approximated in our QGE formulation, only the conservation of kinetic energy is relevant to our setting. We emphasize, however, that one can use the streamfunction approximation to derive a potential vorticity approximation (see, e.g., [19]). In that case, the other two conservation properties of the FE discretization could also be investigated. It is a straightforward calculation (similar to that in Section 5.1 in [11]) to show that our FE discretization does preserve the kinetic energy. Indeed, adding the time derivative information to Eq. (27), neglecting the viscous effects (i.e., discarding the $a_0(\cdot,\cdot)$ term in (27)), neglecting the forcing term (i.e., discarding the $\ell(\cdot)$ term in (27)), and using (29) and (30), one can easily see that the kinetic energy is conserved by our FE discretization.

In order to develop a conforming FEM for the QGE (16), we need to construct subspaces of $H_0^2(\Omega)$, i.e., to find $C^1$ FEs, such as the Argyris triangular element, the Bell triangular element, the Hsieh-Clough-Tocher triangular element (a macroelement), or the Bogner-Fox-Schmit rectangular element [50,19,51,52]. In what follows, we will use the *Argyris FE*. The Argyris FE employs piecewise polynomials of degree five and has twenty-one *degrees of freedom (DOFs)*: the value at each vertex, the value of the first derivatives at each vertex, the value of the second derivatives at each vertex, the value of the mixed derivative at each vertex, and the value of the normal derivatives at each of the edge midpoints. To maintain the direction of the normal derivatives in the transformation from the reference element to the physical element, we use the approach developed in [53].

By using Theorem 6.1.1 and inequality (6.1.5) in [50], we obtain the following three approximation properties for the Argyris FE space $X^h$:

$$\forall\,\chi \in H^6(\Omega)\cap H_0^2(\Omega),\ \exists\,\chi^h \in X^h \quad \text{such that} \quad \|\chi-\chi^h\|_2 \leqslant C h^4 |\chi|_6, \tag{31}$$

$$\forall\,\chi \in H^4(\Omega)\cap H_0^2(\Omega),\ \exists\,\chi^h \in X^h \quad \text{such that} \quad \|\chi-\chi^h\|_2 \leqslant C h^2 |\chi|_4, \tag{32}$$

$$\forall\,\chi \in H^3(\Omega)\cap H_0^2(\Omega),\ \exists\,\chi^h \in X^h \quad \text{such that} \quad \|\chi-\chi^h\|_2 \leqslant C h |\chi|_3, \tag{33}$$

where $C$ is a generic constant that can depend on the data, but not on the meshsize $h$. Property (31) follows from (6.1.5) in [50] with $q=2$, $p=2$, $m=2$ and $k+1=6$. Property (32) follows from (6.1.5) in [50] with $q=2$, $p=2$, $m=2$ and $k+1=4$. Finally, property (33) follows from (6.1.5) in [50] with $q=2$, $p=2$, $m=2$ and $k+1=3$.

## 4. Error analysis

The main goal of this section is to develop a rigorous numerical analysis for the FE discretization of the QGE (27) by using the conforming Argyris element. In Theorem 3, we prove error estimates in the $H^2$ norm by using an approach similar to that used in [45]. In Theorem 4, we prove error estimates in the $L^2$ and $H^1$ norms by using a duality argument.

**Theorem 3.** *Let $\psi$ be the solution of (16) and $\psi^h$ be the solution of (27). Furthermore, assume that the following small data condition is satisfied:*

$$Re^{-2}\,Ro \geqslant \Gamma_1\,\|F\|_{-2}, \tag{34}$$

*where Re is the Reynolds number defined in (9), Ro is the Rossby number defined in (8), $\Gamma_1$ is the continuity constant of the trilinear form $a_1$ in (18), and F is the forcing term. Then the following error estimate holds:*

$$|\psi-\psi^h|_2 \leqslant C(Re,Ro,\Gamma_1,\Gamma_2,F)\inf_{\chi^h\in X^h}|\psi-\chi^h|_2, \tag{35}$$

*where $\Gamma_2$ is the continuity constant of the bilinear form $a_2$ in (19) and*

$$C(Re,Ro,\Gamma_1,\Gamma_2,F) := \frac{Ro^{-1}\,\Gamma_2 + 2\,Re^{-1} + \Gamma_1\,Re\,Ro^{-1}\,\|F\|_{-2}}{Re^{-1} - \Gamma_1\,Re\,Ro^{-1}\,\|F\|_{-2}} \tag{36}$$

*is a generic constant that can depend on $Re, Ro, \Gamma_1, \Gamma_2, F$, but not on the meshsize h.*

**Remark 3.** Note that the small data condition in Theorem 3 involves *both* the Reynolds number and the Rossby number, the latter quantifying the rotation effects in the QGE.

Furthermore, note that the standard small data condition $Re^{-2} \geqslant \Gamma_1\,\|F\|_{-2}$ used to prove the uniqueness for the steady-state 2D NSE [20,21,46,49] is significantly more restrictive for the QGE,

since (34) has the Rossby number (which is small when rotation effects are significant) on the left-hand side. This is somewhat counterintuitive, since in general rotation effects are expected to help in proving the well-posedness of the system. We think that the explanation is the following: Rotation effects do make the mathematical analysis of 3D flows more amenable by giving them a 2D character. We, however, are concerned with 2D flows (the QGE). In this case, the small data condition (34) (needed in proving the uniqueness of the solution) indicates that rotation effects make the mathematical analysis of the (2D) QGE more complicated than that of the 2D NSE.

Finally, we note that, just as in the NSE case, the theoretical small data condition (34) is often too restrictive in practical (time-dependent) computations, and thus is generally ignored. For a detailed discussion of the small data condition in the NSE case, the reader is referred to Chapter 6 in [46] (see also [49,20,21,54]).

**Proof.** Since $X^h \subset X$, (16) holds for all $\chi = \chi^h \in X^h$. Subtracting (27) from (16) with $\chi = \chi^h \in X^h$ gives

$$a_0(\psi - \psi^h, \chi^h) + a_1(\psi, \psi, \chi^h) - a_1(\psi^h, \psi^h, \chi^h) + a_2(\psi - \psi^h, \chi^h) = 0 \quad \forall \chi^h \in X^h. \tag{37}$$

Next, adding and subtracting $a_1(\psi^h, \psi, \chi^h)$ to (37), we get

$$a_0(\psi - \psi^h, \chi^h) + a_1(\psi, \psi, \chi^h) - a_1(\psi^h, \psi, \chi^h) + a_1(\psi^h, \psi, \chi^h) - a_1(\psi^h, \psi^h, \chi^h) + a_2(\psi - \psi^h, \chi^h) = 0 \quad \forall \chi^h \in X^h. \tag{38}$$

The error $e$ can be decomposed as $e := \psi - \psi^h = (\psi - \lambda^h) + (\lambda^h - \psi^h) := \eta + \varphi^h$, where $\lambda^h \in X^h$ is arbitrary. Thus, Eq. (38) can be rewritten as

$$a_0(\eta + \varphi^h, \chi^h) + a_1(\eta + \varphi^h, \psi, \chi^h) + a_1(\psi^h, \eta + \varphi^h, \chi^h) + a_2(\eta + \varphi^h, \chi^h) = 0 \quad \forall \chi^h \in X^h. \tag{39}$$

Letting $\chi^h := \varphi^h$ in (39), we obtain

$$a_0(\varphi^h, \varphi^h) + a_2(\varphi^h, \varphi^h) = -a_0(\eta, \varphi^h) - a_1(\eta, \psi, \varphi^h) - a_1(\varphi^h, \psi, \varphi^h) - a_1(\psi^h, \eta, \varphi^h) - a_1(\psi^h, \varphi^h, \varphi^h) - a_2(\eta, \varphi^h). \tag{40}$$

Note that, since $a_2(\varphi^h, \varphi^h) = -a_2(\varphi^h, \varphi^h)\ \forall \varphi^h \in X^h \subset X = H_0^2$, it follows that $a_2(\varphi^h, \varphi^h) = 0$. We also have that $a_1(\psi^h, \varphi^h, \varphi^h) = 0$. Using these equalities in (40), we get

$$a_0(\varphi^h, \varphi^h) = -a_0(\eta, \varphi^h) - a_1(\eta, \psi, \varphi^h) - a_1(\varphi^h, \psi, \varphi^h) - a_1(\psi^h, \eta, \varphi^h) - a_2(\eta, \varphi^h). \tag{41}$$

Using $a_0(\varphi^h, \varphi^h) = Re^{-1} |\varphi^h|_2^2$ and (12)–(14) in (41), simplifying, and rearranging terms, gives

$$|\varphi^h|_2 \leqslant \left(Re^{-1} - \Gamma_1 |\psi|_2\right)^{-1} \left(Re^{-1} + \Gamma_1 |\psi|_2 + \Gamma_1 |\psi^h|_2 + Ro^{-1} \Gamma_2\right) |\eta|_2. \tag{42}$$

Using (42) and the triangle inequality along with the stability estimates (22) and (28), gives:

$$\begin{aligned} |e|_2 &\leqslant |\eta|_2 + |\varphi^h|_2 \\ &\leqslant \left[1 + \frac{Re^{-1} + \Gamma_1 |\psi|_2 + \Gamma_1 |\psi^h|_2 + Ro^{-1} \Gamma_2}{Re^{-1} - \Gamma_1 |\psi|_2}\right] |\eta|_2 \\ &= \left[\frac{Ro^{-1} \Gamma_2 + 2 Re^{-1} + \Gamma_1 Re\, Ro^{-1} \|F\|_{-2}}{Re^{-1} - \Gamma_1 Re\, Ro^{-1} \|F\|_{-2}}\right] |\psi - \lambda^h|_2, \end{aligned} \tag{43}$$

where $\lambda^h \in X^h$ is arbitrary. We note that the small data condition (34) ensures the positivity of the RHS of (43). Taking the infimum over $\lambda^h \in X^h$ in (43) proves estimate (35). □

Next, we prove error estimates in the $L^2$ norm and $H^1$ seminorm by using a duality argument. To this end, we first notice that the QGE (10) can be written as

$$\mathcal{N}\psi = Ro^{-1} F, \tag{44}$$

where the nonlinear operator $\mathcal{N}$ is defined on $X = H_0^2(\Omega)$ as

$$\mathcal{N}\psi := Re^{-1} \Delta^2 \psi + J(\psi, \Delta\psi) - Ro^{-1} \frac{\partial \psi}{\partial x}. \tag{45}$$

The linearization of $\mathcal{N}$ around $\psi$, a solution of (10), yields the following *linear* operator, which is defined on $X = H_0^2(\Omega)$:

$$\mathcal{L}\chi := Re^{-1} \Delta^2 \chi + J(\chi, \Delta\psi) + J(\psi, \Delta\chi) - Ro^{-1} \frac{\partial \chi}{\partial x}. \tag{46}$$

To find the *dual operator* $\mathcal{L}^*$ of $\mathcal{L}$, we use (46) and apply Green's theorem:

$$\begin{aligned} (\mathcal{L}\chi, \psi^*) &= \left(Re^{-1} \Delta^2 \chi + J(\chi, \Delta\psi) + J(\psi, \Delta\chi) - Ro^{-1} \frac{\partial \chi}{\partial x}, \psi^*\right) \\ &= \left(\chi, Re^{-1} \Delta^2 \psi^* - J(\psi, \Delta\psi^*) + Ro^{-1} \frac{\partial \psi^*}{\partial x}\right) + (\chi, J(\Delta\psi, \psi^*)) \\ &= (\chi, \mathcal{L}^* \psi^*). \end{aligned} \tag{47}$$

Thus, the dual operator $\mathcal{L}^*$, which is defined on $X = H_0^2(\Omega)$, is given by

$$\mathcal{L}^* \psi^* = Re^{-1} \Delta^2 \psi^* - J(\psi, \Delta\psi^*) + J(\Delta\psi, \psi^*) + Ro^{-1} \frac{\partial \psi^*}{\partial x}. \tag{48}$$

For any given $g \in L^2(\Omega)$, the weak formulation of the *dual problem* is:

$$(\mathcal{L}^* \psi^*, \chi) = (g, \chi) \quad \forall \chi \in X = H_0^2(\Omega). \tag{49}$$

We assume that $\psi^*$, the solution of (49), satisfies the following elliptic regularity estimates:

$$\psi^* \in H^4(\Omega) \cap H_0^2(\Omega), \tag{50}$$

$$\|\psi^*\|_4 \leqslant C \|g\|_0, \tag{51}$$

$$\|\psi^*\|_3 \leqslant C \|g\|_{-1}, \tag{52}$$

where $C$ is a generic constant that can depend on the data, but not on the meshsize $h$.

**Remark 4.** We note that this type of elliptic regularity was also assumed in [45] for the streamfunction formulation of the 2D NSE. In that report, it was also noted that, for a polygonal domain with maximum interior vertex angle $\theta < 126°$, the assumed elliptic regularity was actually proved in [55]. We note that the theory developed in [55] carries over to our case. In Section 5 in [55] it is proved that, for weakly nonlinear problems that involve the biharmonic operator as linear main part and that satisfy certain growth restrictions, each weak solution satisfies elliptic regularity results of the form (50)–(52). Assuming that $\Omega$ is a bounded polygonal domain with inner angle $\omega$ at each boundary corner satisfying $\omega < 126.283696\ldots°$, Theorem 7 in [55] with $k = 0$ and $k = 1$ implies (50)–(52). Using an argument similar to that used in Section 6(b) in [55] to prove that the streamfunction formulation of the 2D NSE satisfies the restrictions in Theorem 7, we can prove that $\psi^*$, the solution of our dual problem (49), satisfies the elliptic regularity results in (50)–(52). Indeed, the main point in Section 6(b) in [55] is that the corner singularities arising in flows around sharp corners are essentially determined by the linear main part $\Delta^2$ in the streamfunction formulation of the 2D NSE, which is the linear main part of our dual problem (49) as well.

**Theorem 4.** *Let $\psi$ be the solution of (16) and $\psi^h$ be the solution of (27). Assume that the same small data condition as in Theorem 3 is satisfied:*

$$Re^{-2}\,Ro \geqslant \Gamma_1 \|F\|_{-2}. \tag{53}$$

*Furthermore, assume that $\psi \in H^6(\Omega) \cap H_0^2(\Omega)$. Then there exist positive constants $C_0$, $C_1$ and $C_2$ that can depend on $Re, Ro, \Gamma_1, \Gamma_2, F$, but not on the meshsize $h$, such that*

$$|\psi - \psi^h|_2 \leqslant C_2 h^4, \tag{54}$$

$$|\psi - \psi^h|_1 \leqslant C_1 h^5, \tag{55}$$

$$\|\psi - \psi^h\|_0 \leqslant C_0 h^6. \tag{56}$$

**Remark 5.** The Argyris FE error estimates in Theorem 4 can be extended to other conforming $C^1$ FE spaces.

**Proof.** Estimate (54) follows immediately from (31) and Theorem 3. Estimates (56) and (55) follow from a duality argument.

The error in the primal problem (16) and the interpolation error in the dual problem (49) (with the function $g$ to be specified later) are denoted as $e := \psi - \psi^h$ and $e^* := \psi^* - \psi^{*h}$, respectively.

To prove the $L^2$ norm estimate (56), we consider $g = e$ in the dual problem (49):

$$\begin{aligned}|e|^2 &= (e,e) = (\mathcal{L}e, \psi^*) = (e, \mathcal{L}^*\psi^*) = (e, \mathcal{L}^* e^*) + (e, \mathcal{L}^*\psi^{*h}) \\ &= (\mathcal{L}e, e^*) + (\mathcal{L}e, \psi^{*h}).\end{aligned} \tag{57}$$

The last term on the right-hand side of (57) is given by

$$(\mathcal{L}e, \psi^{*h}) = \left(Re^{-1}\Delta^2 e + J(e, \Delta\psi) + J(\psi, \Delta e) - Ro^{-1}\frac{\partial e}{\partial x}, \psi^{*h}\right). \tag{58}$$

To estimate this term, we consider the error equation obtained by subtracting (27) (with $\psi^h = \psi^{*h}$) from (16) (with $\chi = \psi^{*h}$):

$$\begin{aligned}&\left(Re^{-1}\Delta^2 e - Ro^{-1}\frac{\partial e}{\partial x}, \psi^{*h}\right) + \left(J(\psi, \Delta\psi) - J(\psi^h, \Delta\psi^h), \psi^{*h}\right) \\ &= 0.\end{aligned} \tag{59}$$

Using (59), Eq. (58) can be written as follows:

$$(\mathcal{L}e, \psi^{*h}) = \left(J(e, \Delta\psi) + J(\psi, \Delta e) - J(\psi, \Delta\psi) + J(\psi^h, \Delta\psi^h), \psi^{*h}\right). \tag{60}$$

Thus, by using (60), Eq. (57) becomes

$$\begin{aligned}|e|^2 &= (\mathcal{L}e, e^*) + (\mathcal{L}e, \psi^{*h}) \\ &= a_0(e, e^*) + a_2(e, e^*) + a_1(e, \psi, e^*) + a_1(\psi, e, e^*) \\ &\quad + a_1(e, \psi, \psi^{*h}) + a_1(\psi, e, \psi^{*h}) - a_1(\psi, \psi, \psi^{*h}) \\ &\quad + a_1(\psi^h, \psi^h, \psi^{*h}) \\ &= a_0(e, e^*) + a_2(e, e^*) + a_1(e, \psi, e^*) + a_1(\psi, e, e^*) \\ &\quad - a_1(e, \psi, e^*) + a_1(e, \psi^h, e^*) + a_1(e, e, \psi^*).\end{aligned} \tag{61}$$

Using the bounds in (17)–(19), (61) yields

$$\begin{aligned}|e|^2 &\leqslant Re^{-1}|e|_2|e^*|_2 + Ro^{-1}\Gamma_2|e|_2|e^*|_2 + \Gamma_1|e|_2|\psi|_2|e^*|_2 \\ &\quad + \Gamma_1|\psi|_2|e|_2|e^*|_2 + \Gamma_1|e|_2|\psi|_2|e^*|_2 + \Gamma_1|e|_2|\psi^h|_2|e^*|_2 \\ &\quad + \Gamma_1|e|_2|e|_2|\psi^*|_2 = |e|_2|e^*|_2\left(Re^{-1} + Ro^{-1}\Gamma_2 + \Gamma_1|\psi|_2 + \Gamma_1|\psi|_2\right. \\ &\quad \left.+\Gamma_1|\psi|_2 + \Gamma_1|\psi^h|_2\right) + |e|_2^2(\Gamma_1|\psi^*|_2).\end{aligned} \tag{62}$$

Using the stability estimates (22) and (28), (62) becomes

$$|e|^2 \leqslant C|e|_2|e^*|_2 + |e|_2^2(\Gamma_1|\psi^*|_2), \tag{63}$$

where $C$ is a generic constant that can depend on $Re, Ro, \Gamma_1, \Gamma_2, F$, but *not* on the meshsize $h$. Using the approximation results (32), we get

$$|e^*|_2 \leqslant Ch^2|\psi^*|_4. \tag{64}$$

Using (50)–(51), the elliptic regularity results of the dual problem (49) with $g := e$, we get

$$|\psi^*|_4 \leqslant C|e|, \tag{65}$$

which obviously implies

$$|\psi^*|_2 \leqslant C|e|. \tag{66}$$

Inequalities (64)–(65) imply

$$|e^*|_2 \leqslant Ch^2|e|. \tag{67}$$

Inserting (66) and (67) in (63), we get

$$|e|^2 \leqslant Ch^2|e|_2|e| + C|e|_2^2|e|. \tag{68}$$

Using the obvious simplifications and the $H^2$ error estimate (54) in (68) yields

$$|e| \leqslant Ch^2|e|_2 + C|e|_2^2 \leqslant Ch^6 + Ch^8 = C_0h^6, \tag{69}$$

which proves the $L^2$ error estimate (56).

Estimate (55) can be proven using the same duality argument as that used to prove estimate (56). The major differences are that we use $g = -\Delta e$ in the dual problem (49) and we use the approximation result (33). □

## 5. Numerical results

The main goal of this section is twofold. First, we show that the FE discretization of the streamfunction formulation of the QGE (27) with the Argyris element produces accurate numerical approximations, which are close to those in the published literature [10,9,4]. Second, we show that the numerical results follow the theoretical error estimates in Theorem 3 and Theorem 4. The mathematical models used in the numerical investigation are presented in Section 5.1. The numerical tests in which both the accuracy and the convergence rates of the FE discretization are investigated are presented in Section 5.2.

### 5.1. Mathematical models

Although the pure streamfunction formulation of the steady QGE (10) is our main concern, we also test our Argyris FE discretization on two simplified settings: (i) the *linear Stommel* model; and (ii) the *linear Stommel–Munk* model. The reason for using these two additional numerical tests is that they are standard test problems in the geophysical fluid dynamics literature (see, e.g., Chapter 14 in Vallis [4] as well as the reports of Myers and Weaver [9] and Cascon et al. [10]). This allows us to benchmark our numerical results against those in the published literature. Since both the linear Stommel and the linear Stommel–Munk models lack the nonlinearity present in the QGE (10), they represent good stepping stones for testing our FE discretization.

The *linear Stommel–Munk* model (see Eq. (14.42) in [4] and Problem 2 in [10]) is

$$\epsilon_S\Delta\psi - \epsilon_M\Delta^2\psi + \frac{\partial\psi}{\partial x} = f. \tag{70}$$

The parameters $\epsilon_S$ and $\epsilon_M$ in (70) are the *Stommel number* and *Munk scale*, respectively, which are given by (see, e.g., Eq. (10)

in [9] and Eqs. (14.22) and (14.44) in [4]) $\epsilon_M = \frac{A}{\beta L^3}$ and $\epsilon_S = \frac{\gamma}{\beta L}$, where $A$ is the eddy viscosity parameterization, $\beta$ is the coefficient multiplying the $y$ coordinate in the $\beta$-plane approximation, $L$ is the width of the computational domain, and $\gamma$ is the coefficient of the linear drag (Rayleigh friction) as might be generated by a bottom Ekman layer (see Eq. (14.5) in [4]). The model is supplemented with appropriate boundary conditions, which will be described for each of the subsequent numerical tests.

We note that the linear Stommel–Munk model (70) is similar in form to the QGE (10). Indeed, both models contain the biharmonic operator $\Delta^2\psi$, the rotation term $\frac{\partial\psi}{\partial x}$, and the forcing term $f$. The two main differences between the two models are the following: First, the QGE are nonlinear, since they contain the Jacobian term $J(\psi, q)$, whereas the Stommel–Munk model is linear. The second difference is that the linear Stommel–Munk model contains a Laplacian term $\Delta\psi$, whereas the QGE do not.

We also note that the two models use different parameters: the Reynolds number, $Re$, and the Rossby number, $Ro$, in the QGE and the Stommel number, $\epsilon_S$, and the Munk scale, $\epsilon_M$, in the linear Stommel–Munk model. The parameters $\epsilon_M, Ro$, and $Re$ are related through $\epsilon_M = Ro\,Re^{-1}$. There is, however, no explicit relationship among $\epsilon_S, Ro$, and $Re$. The reason is that the QGE (10) do not contain the Laplacian term that is present in the Stommel–Munk model (70), which models the bottom Rayleigh friction. Thus, the coefficient $\gamma$ does not have a counterpart in the QGE. This explains why $\epsilon_S$, which depends on $\gamma$, cannot be directly expressed as a function of $Ro$ and $Re$.

The second simplified model used in our numerical investigation is the *linear Stommel* model (see, e.g., Eq. (14.22) in [4] and Eq. (11) in [9]):

$$\epsilon_S\Delta\psi + \frac{\partial\psi}{\partial x} = f. \tag{71}$$

We note that the linear Stommel model (71) is just the linear Stommel–Munk model (70) in which the biharmonic term is dropped (i.e., $\epsilon_M = 0$).

### 5.2. Numerical tests

In this section, we present results for the linear Stommel model (71), the linear Stommel–Munk model (70), and the (nonlinear) QGE (10).

#### 5.2.1. Linear Stommel model

This section presents the results for the FE discretization of the linear Stommel model (71) by using the Argyris element. The computational domain is $\Omega = [0,1]\times[0,1]$. For completeness, we present results for two numerical tests. The first test, denoted by Test 1, corresponds to the exact solution used by Vallis (Eq. (14.38) in [4]), while the second test, denoted by Test 2, corresponds to the exact solution used by Myers and Weaver (Eqs. (15) and (16) in [9]).

**Test 1a:** In this test, we choose the same setting as that used in Eq. (14.38) in [4]. In particular, the forcing term and the non-homogeneous Dirichlet boundary conditions are chosen to match those given by the exact solution $\psi(x,y) = (1 - x - e^{-x/\epsilon_S})\,\pi\sin(\pi y)$. We choose the same Stommel number as that used in [4], i.e., $\epsilon_S = 0.04$.

Fig. 1(a) presents the streamlines of the approximate solution obtained by using the Argyris element on a mesh with $h = \frac{1}{32}$ and 9670 DoFs. We note that Fig. 1(a) resembles Fig. 14.5 in [4]. Since the exact solution is available, we can compute the errors in various norms. Table 1 presents the errors $e_0, e_1$, and $e_2$ (i.e., the $L^2, H^1$, and $H^2$ errors, respectively) for various values of the mesh-size, $h$ (the DoFs are also included). We note that the errors in Table 1 follow the theoretical rates of convergence predicted by the estimates (54)–(56) in Theorem 4. The orders of convergence in Table 1 are close to the theoretical ones for the fine meshes, but not as close for the coarse meshes. We think that the inaccuracies on the coarse meshes are due to their inability to capture the thin boundary layer at $x = 0$. The finer the mesh gets, the better this boundary layer is captured and the better the numerical accuracy becomes. We also note that similar inaccuracies near the boundary layer were observed in the numerical experiments in [10].

**Test 1b:** To verify whether the degrading accuracy of the approximation is indeed due to the thin (western) boundary layer, we use $\epsilon_S = 1$ in Test 1a, which will result in a much thicker western boundary layer. We then run Test 1a, but with the new $\epsilon_S$. As can be seen in Table 2, the rates of convergence are the expected theoretical orders of convergence. This shows that the reason for the inaccuracies in Table 1 were indeed due to the thin western boundary layer.

**Test 2:** For this test, we use the exact solution given by Eqs. (15) and (16) in [9], i.e.,

$$\psi(x,y) = \frac{\sin(\pi y)}{\pi(1+4\pi^2\epsilon_S^2)}\Big\{2\pi\epsilon_S\sin(\pi x) + \cos(\pi x) + \frac{1}{e^{R_1} - e^{R_2}}\left[(1+e^{R_2})e^{R_1 x} - (1+e^{R_1})e^{R_2 x}\right]\Big\},$$

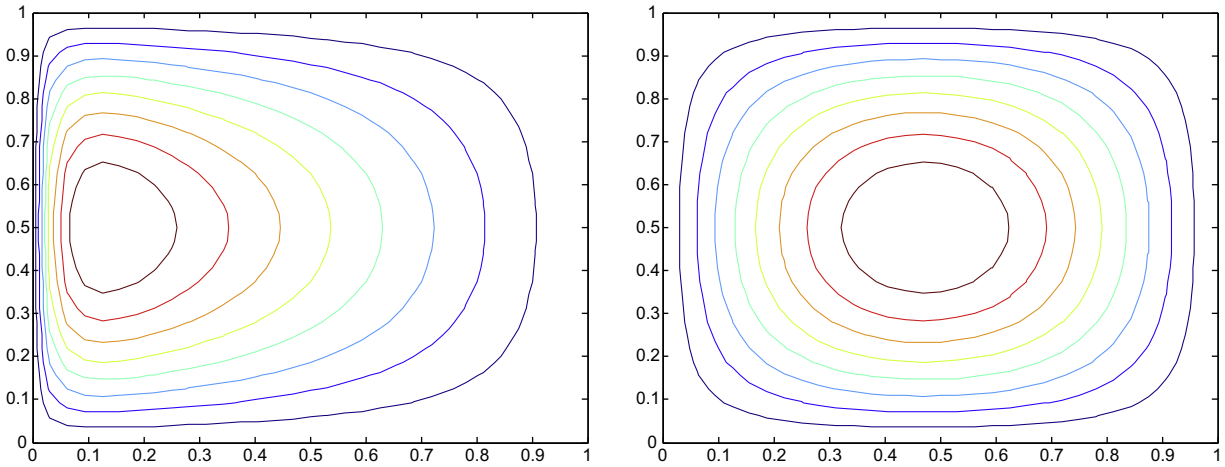


(a) Test 1a [4]. (b) Test 1b [4].

**Fig. 1.** Linear Stommel model (71): Streamlines of the approximation, $\psi^h$, on a mesh with $h = \frac{1}{32}$.

**Table 1**
Linear Stommel model (71), Test 1a [4]: The errors $e_0, e_1, e_2$ for various meshsizes h.

| $h$ | *DoFs* | $e_0$ | $L^2$ order | $e_1$ | $H^1$ order | $e_2$ | $H^2$ order |
|---|---|---|---|---|---|---|---|
| 1/2 | 70 | 0.1148 | – | 1.81 | – | 83.67 | – |
| 1/4 | 206 | 0.01018 | 3.495 | 0.312 | 2.537 | 25.48 | 1.716 |
| 1/8 | 694 | 0.0004461 | 4.512 | 0.02585 | 3.593 | 3.902 | 2.707 |
| 1/16 | 2534 | $1.09 \times 10^{-5}$ | 5.355 | 0.001215 | 4.412 | 0.3494 | 3.481 |
| 1/32 | 9670 | $1.972 \times 10^{-7}$ | 5.788 | $4.349 \times 10^{-5}$ | 4.804 | 0.02335 | 3.903 |

**Table 2**
Linear Stommel model (71), Test 1b [4]: The errors $e_0, e_1, e_2$ for various meshsizes $h$.

| $h$ | *DoFs* | $e_0$ | $L^2$ order | $e_1$ | $H^1$ order | $e_2$ | $H^2$ order |
|---|---|---|---|---|---|---|---|
| 1/2 | 70 | $1.689 \times 10^{-5}$ | - | 0.0003434 | – | 0.008721 | – |
| 1/4 | 206 | $3.722 \times 10^{-7}$ | 5.504 | $1.341 \times 10^{-5}$ | 4.678 | 0.0005616 | 3.957 |
| 1/8 | 694 | $4.891 \times 10^{-9}$ | 6.25 | $3.757 \times 10^{-7}$ | 5.158 | $3.25 \times 10^{-5}$ | 4.111 |
| 1/16 | 2534 | $7.079 \times 10^{-11}$ | 6.111 | $1.117 \times 10^{-8}$ | 5.071 | $1.964 \times 10^{-6}$ | 4.049 |
| 1/32 | 9670 | $1.08 \times 10^{-12}$ | 6.035 | $3.437 \times 10^{-10}$ | 5.023 | $1.213 \times 10^{-7}$ | 4.018 |

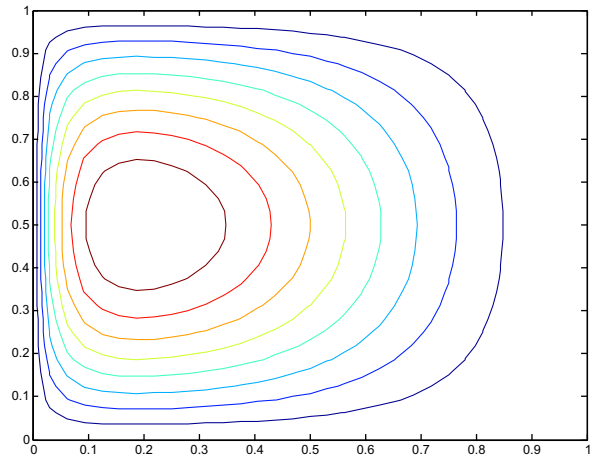


**Fig. 2.** Linear Stommel model (71), Test 2 [9]: Streamlines of the approximation, $\psi^h$, on a mesh with $h = \frac{1}{32}$ and 9670 DoFs.

where $R_{1,2} = \frac{-1 \pm \sqrt{1+4\pi^2\epsilon_S^2}}{2\epsilon_S}$. The forcing and the homogeneous Dirichlet boundary conditions are chosen to match those given by the exact solution. We choose the same Stommel number as that used in [9], i.e., $\epsilon_S = 0.05$.

Fig. 2 presents the streamlines of the approximate solution obtained by using the Argyris element on a mesh with $h = \frac{1}{32}$ and 9670 DoFs. We note that Fig. 2 resembles Fig. 2 in [9]. Table 3 presents the errors $e_0$, $e_1$, and $e_2$ for various meshsizes $h$. The errors in Table 3 follow the theoretical rates of convergence predicted by the estimates (54)–(56) in Theorem 4. Again, we see that the orders of convergence in Table 3 are close to the theoretical ones for the fine meshes, but not as close for the coarse meshes. We again attribute this to the inaccuracies at the thin (western) boundary layer at $x = 0$.

*5.2.2. Linear Stommel–Munk model*

This section presents results for the FE discretization of the linear Stommel–Munk model (70) by using the Argyris element. Our computational setting is the same as that used by Cascon et al. [10]: The computational domain is $\Omega = [0,3] \times [0,1]$, the Munk scale is $\epsilon_M = 6 \times 10^{-5}$, the Stommel number is $\epsilon_S = 0.05$, and the boundary conditions are $\psi = \frac{\partial \psi}{\partial \mathbf{n}} = 0$ on $\partial\Omega$. For completeness, we present results for two numerical tests, denoted by Test 3 and Test 4, corresponding to Test 1 and Test 2 in [10], respectively.

**Test 3:** For this test, we use the exact solution given by Test 1 in [10], i.e., $\psi(x,y) = \sin^2\left(\frac{\pi x}{3}\right)\sin^2(\pi y)$. The forcing term is chosen to match that given by the exact solution.

Fig. 3(a) presents the streamlines of the approximate solution obtained by using the Argyris element on a mesh with $h = \frac{1}{32}$ and 28550 DoFs. We note that Fig. 3(a) resembles Fig. 7 in [9]. Table 4 presents the errors $e_0$, $e_1$, and $e_2$ for various meshsizes $h$. The errors in Table 4 follow the theoretical rates of convergence predicted by the estimates (54)–(56) in Theorem 4. This time, we see that the orders of convergence in Table 4 are close to the theoretical ones for the fine meshes, but are higher than expected for the coarse meshes. We attribute this to the fact that the exact solution does not display any boundary layers that could be challenging to capture by the Argyris element on a coarse mesh.

**Test 4:** For this test, we use the exact solution given by Test 2 in [10], i.e., $\psi(x,y) = \left[\left(1 - \frac{x}{3}\right)\left(1 - e^{-20x}\right)\sin(\pi y)\right]^2$. We take the forcing term $f$ corresponding to the exact solution.

Fig. 3(b) presents the streamlines of the approximate solution obtained by using the Argyris element on a mesh with $h = \frac{1}{32}$ and 28550 DoFs. We note that Fig. 3(b) resembles Fig. 10 in [9]. Table 5 presents the errors $e_0$, $e_1$, and $e_2$ for various meshsizes $h$. We note that the errors in Table 5 follow the theoretical rates of convergence predicted by the estimates (54)–(56) in Theorem 4. Again, we see that the orders of convergence in Table 5 are close to the theoretical ones for the fine meshes, but not as close for the coarse

**Table 3**
Linear Stommel model (71), Test 2 [9]: The errors $e_0, e_1, e_2$ for various meshsizes $h$.

| $h$ | *DoFs* | $e_0$ | $L^2$ order | $e_1$ | $H^1$ order | $e_2$ | $H^2$ order |
|---|---|---|---|---|---|---|---|
| 1/2 | 70 | 0.005645 | – | 0.1451 | – | 6.602 | – |
| 1/4 | 206 | 0.0004276 | 3.723 | 0.02081 | 2.801 | 1.632 | 2.016 |
| 1/8 | 694 | $1.46 \times 10^{-5}$ | 4.872 | 0.001408 | 3.886 | 0.2066 | 2.982 |
| 1/16 | 2534 | $2.954 \times 10^{-7}$ | 5.627 | $5.829 \times 10^{-5}$ | 4.594 | 0.0165 | 3.646 |
| 1/32 | 9670 | $4.968 \times 10^{-9}$ | 5.894 | $1.998 \times 10^{-6}$ | 4.867 | 0.001069 | 3.948 |

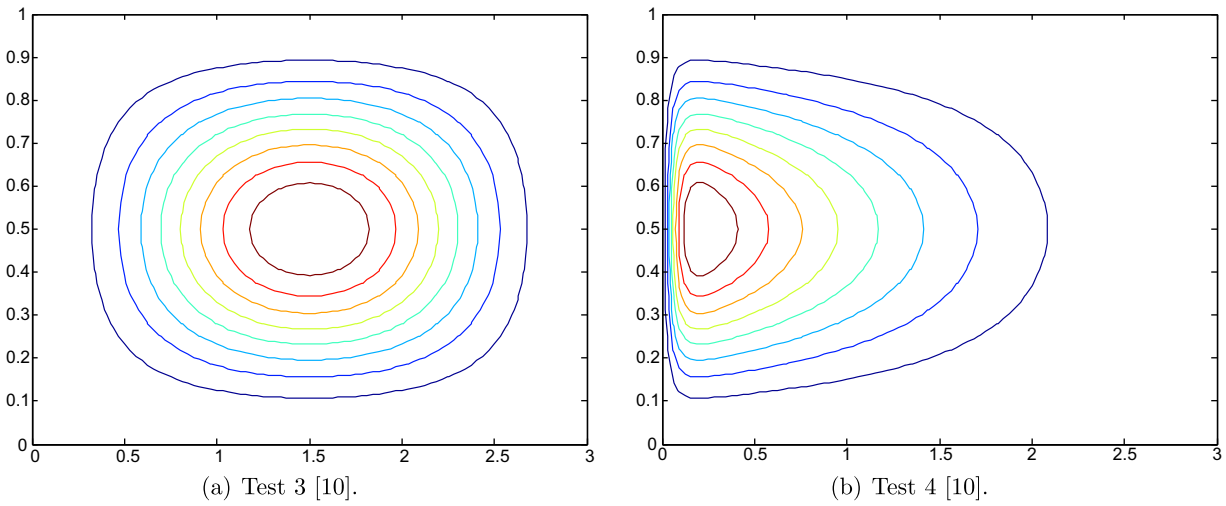


**Fig. 3.** Linear Stommel–Munk Model (70): Streamlines of the approximation, $\psi^h$, on a mesh with $h = \frac{1}{32}$ and 28550 DoFs.

**Table 4**
Linear Stommel–Munk Model (70), Test 3 [10]: The errors $e_0, e_1, e_2$ for various meshsizes $h$.

| $h$ | DoFs | $e_0$ | $L^2$ order | $e_1$ | $H^1$ order | $e_2$ | $H^2$ order |
|---|---|---|---|---|---|---|---|
| 1/2 | 170 | 0.00299 | – | 0.04084 | – | 0.7624 | – |
| 1/4 | 550 | $3.217 \times 10^{-5}$ | 6.539 | 0.001031 | 5.308 | 0.04078 | 4.225 |
| 1/8 | 1958 | $3.437 \times 10^{-7}$ | 6.548 | $2.491 \times 10^{-5}$ | 5.371 | 0.002253 | 4.178 |
| 1/16 | 7366 | $4.571 \times 10^{-9}$ | 6.232 | $7.026 \times 10^{-7}$ | 5.148 | 0.0001344 | 4.067 |
| 1/32 | 28550 | $6.704 \times 10^{-11}$ | 6.091 | $2.113 \times 10^{-8}$ | 5.056 | $8.26 \times 10^{-6}$ | 4.024 |

**Table 5**
Linear Stommel–Munk Model (70), Test 4 [10]: The errors $e_0, e_1, e_2$ for various meshsizes $h$.

| $h$ | DoFs | $e_0$ | $L^2$ order | $e_1$ | $H^1$ order | $e_2$ | $H^2$ order |
|---|---|---|---|---|---|---|---|
| 1/2 | 170 | 0.06036 | - | 1.162 | - | 38.99 | - |
| 1/4 | 550 | 0.01132 | 2.414 | 0.3995 | 1.541 | 21.4 | 0.8656 |
| 1/8 | 1958 | 0.0008399 | 3.753 | 0.05914 | 2.756 | 5.656 | 1.92 |
| 1/16 | 7366 | $2.817 \times 10^{-5}$ | 4.898 | 0.004008 | 3.883 | 0.7378 | 2.939 |
| 1/32 | 28550 | $5.587 \times 10^{-7}$ | 5.656 | 0.0001607 | 4.641 | 0.0597 | 3.627 |

meshes. As stated previously, we attribute this to the inaccuracies at the thin (western) boundary layer at $x = 0$.

*5.2.3. Quasi-geostrophic equations - rectangular domains*

This section presents results for the FE discretization of the streamfunction formulation of the QGE (10) in rectangular domains by using the Argyris element. To solve the resulting nonlinear system of equations, we use Newton's method with the following stopping criteria: the maximum residual norm is $10^{-8}$, the maximum streamfunction iteration increment is $10^{-8}$, and the maximum number of iterations is 10. Our computational domain is $\Omega = [0, 3] \times [0, 1]$, the Reynolds number is $Re = 1.667$, and the Rossby number is $Ro = 10^{-4}$. For completeness, we present results for two numerical tests, denoted by Test 5 and Test 6, corresponding to the exact solutions given in Test 1 and Test 2 of [10], respectively.

**Test 5:** In this test, we take the same exact solution as that in Test 1 of [10], i.e., $\psi(x, y) = \sin^2\left(\frac{\pi x}{3}\right) \sin^2(\pi y)$. The forcing term and homogeneous boundary conditions correspond to the exact solution.

Fig. 4(a) presents the streamlines of the approximate solution obtained by using the Argyris element on a mesh with $h = \frac{1}{32}$ and 28550 DoFs. We note that Fig. 4(a) resembles Fig. 7 in [10]. Table 6 presents the errors $e_0, e_1,$ and $e_2$ for various meshsizes $h$. The errors in Table 6 follow the theoretical rates of convergence predicted by the estimates (54)–(56) in Theorem 4. Again, since the exact solution does not display any boundary layers, we see that the orders of convergence in Table 6 are close to the theoretical ones for the fine meshes, but are higher than expected for the coarse meshes.

**Test 6:** In this test, we take the same exact solution as that in Test 2 of [10], i.e., $\psi(x, y) = \left[\left(1 - \frac{x}{3}\right)\left(1 - e^{-20x}\right) \sin(\pi y)\right]^2$. The forcing term and the homogeneous boundary conditions correspond to the exact solution.

Fig. 4(b) presents the streamlines of the approximate solution obtained by using the Argyris element on a mesh with $h = \frac{1}{32}$ and 28550 DoFs. We note that Fig. 4(b) resembles Fig. 10 in [10]. Table 7 presents the errors $e_0, e_1,$ and $e_2$ for various meshsizes $h$. The errors in Table 7 follow the theoretical rates of convergence predicted by the estimates (54)–(56) in Theorem 4. We see that the orders of convergence in Table 7 are close to the theoretical ones for the fine meshes, but not as close for the coarse meshes. We attribute this to the inaccuracies at the thin boundary layer at $x = 0$.

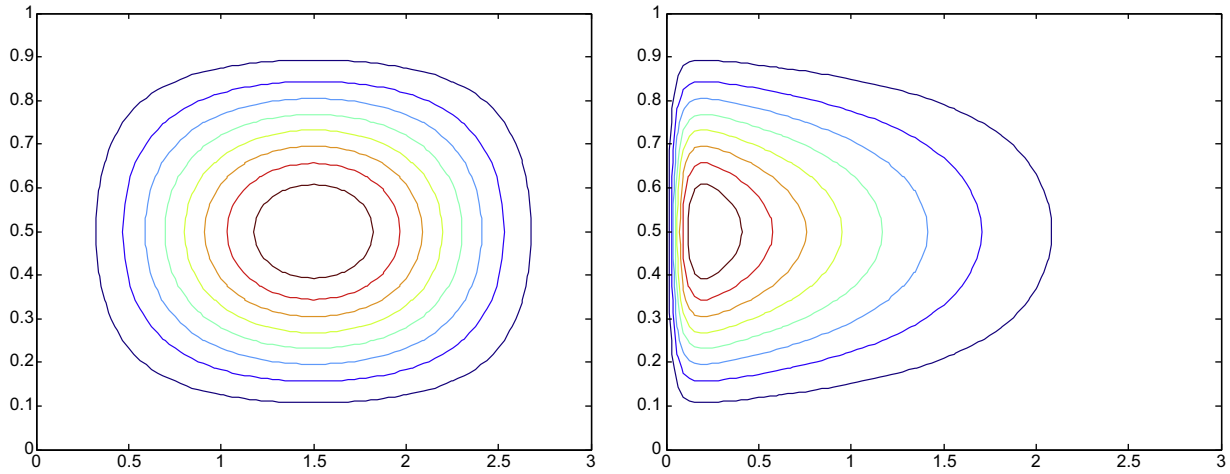

(a) Test 5. (b) Test 6.

**Fig. 4.** QGE (10): Streamlines of the approximation, $\psi^h$, on a mesh with $h = \frac{1}{32}$ and 28550 DoFs.

**Table 6**
QGE (10), Test 5: The errors $e_0, e_1, e_2$ for various meshsizes $h$.

| $h$ | DoFs | $e_0$ | $L^2$ order | $e_1$ | $H^1$ order | $e_2$ | $H^2$ order |
|---|---|---|---|---|---|---|---|
| 1/2 | 170 | 0.005709 | – | 0.06033 | – | 1.087 | – |
| 1/4 | 550 | $3.726 \times 10^{-5}$ | 7.259 | 0.001086 | 5.796 | 0.04113 | 4.724 |
| 1/8 | 1958 | $3.597 \times 10^{-7}$ | 6.695 | $2.534 \times 10^{-5}$ | 5.421 | 0.002252 | 4.191 |
| 1/16 | 7366 | $4.648 \times 10^{-9}$ | 6.274 | $7.065 \times 10^{-7}$ | 5.165 | 0.0001344 | 4.067 |
| 1/32 | 28550 | $6.737 \times 10^{-11}$ | 6.108 | $2.116 \times 10^{-8}$ | 5.061 | $8.26 \times 10^{-6}$ | 4.024 |

**Table 7**
QGE (10), Test 6: The errors $e_0, e_1, e_2$ for various meshsizes $h$.

| $h$ | DoFs | $e_0$ | $L^2$ order | $e_1$ | $H^1$ order | $e_2$ | $H^2$ order |
|---|---|---|---|---|---|---|---|
| 1/2 | 170 | 0.3497 | - | 1.9 | - | 44.05 | - |
| 1/4 | 550 | 0.0302 | 3.533 | 0.4279 | 2.15 | 21.74 | 1.019 |
| 1/8 | 1958 | 0.001507 | 4.324 | 0.06085 | 2.814 | 5.661 | 1.941 |
| 1/16 | 7366 | $3.225 \times 10^{-5}$ | 5.547 | 0.004042 | 3.912 | 0.7379 | 2.94 |
| 1/32 | 28550 | $5.672 \times 10^{-7}$ | 5.829 | 0.000161 | 4.65 | 0.0597 | 3.628 |

*5.2.4. Quasi-geostrophic equations - Mediterranean Sea*

**Test 7:** This section presents results for the FE discretization of the QGE (10) in complex domains by using the Argyris element. As an example of complex computational domain, we chose the Mediterranean Sea [16–18]. We have created a FE mesh of the Mediterranean Sea using GMSH [56]. The coastline data was obtained from NOAA's GSHHS database. Major islands such as Corsica, Sardinia, and Sicily were connected to the nearest land mass in order to ensure a unique streamfunction (see the discussions in [9,19,35,36]). Additionally, the Atlantic Ocean was closed off from the Mediterranean Sea at the Straits of Gibraltar, from the Red Sea at the Suez Canal, and from the Sea of Marmara at the Dardanelles Strait, while the Gulf of Corinth was treated as land. The resultant FE mesh is displayed in Fig. 5. We used a forcing function given by $F(x,y) = \sin\left(\frac{\pi}{4}y\right)$, which is the same forcing function used by Bryan in [57]. We note that Bryan used in [57] a forcing function given by $F(x,y) = \sin\left(\frac{\pi}{2}y\right)$, but on a rectangular domain of height two. Since the height of our computational domain is one, we used a forcing function given by $F(x,y) = \sin\left(\frac{\pi}{4}y\right)$ in order to maintain the same flow structure as that used in [57].

The parameters used in the numerical simulation, which are summarized in Table 8, were the same as those used in [16–18]. By using the parameters in Table 8, we calculated the parameters used in the QGE (10) (i.e., *Ro* and *Re*) as follows: The characteristic velocity scale, $U$, used in the definition of the Rossby number (defined in (8)) is the Sverdrup velocity

$$U := \frac{\pi \tau_0}{\rho H \beta L}, \tag{72}$$

where $\tau_0$ is the amplitude of the wind stress, $\rho$ is the density of the fluid, $H$ is the height of the computational domain, $\beta$ is the coefficient multiplying the $y$ coordinate in the $\beta$-plane approximation, and $L$ is the length of the computational domain. The Sverdrup balance, which was used in the derivation of (72), expresses the balance between the two dominant effects in the system: the $\beta$-effect and the curl of the divergence of the wind stress (see, e.g., Section 14.1.3 in [4]). Using Eq. (2.80) from [4] and the parameters in Table 8 gives the following approximation for the parameter $\beta$:

$$\beta = \frac{2\omega}{r_e}\cos\theta_0 \approx 1.742 \times 10^{-11}\, m^{-1}\, s^{-1}. \tag{73}$$

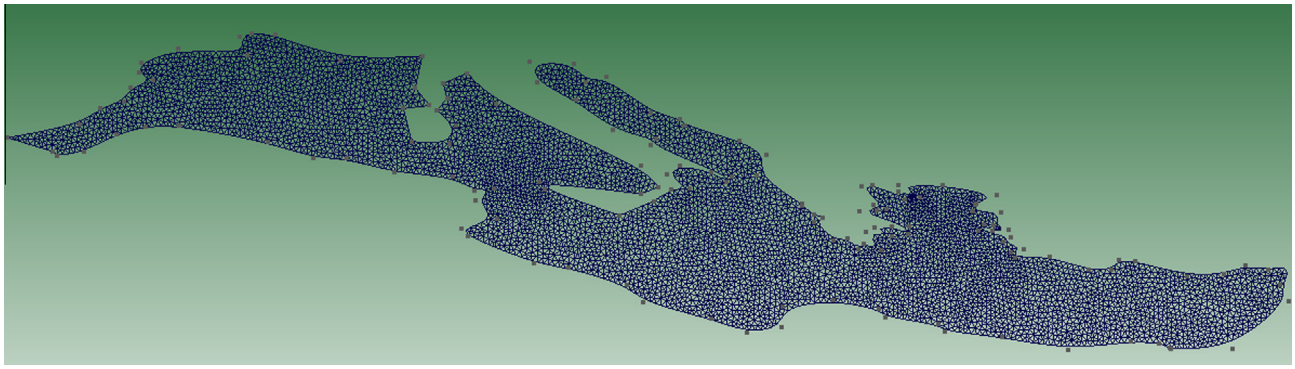

**Fig. 5.** QGE (10), Test 7: Mesh of the Mediterranean Sea with $h = \frac{1}{320}$ and 240342 DoFs.

**Table 8**
QGE (10), Test 7: Parameter values used for the simulations of the Mediterranean Sea [17], where $A, \theta_0, \omega, H, L, r_e, \rho$ are the eddy viscosity, reference angle for the $\beta$-plane approximation, angular velocity of the Earth, domain height, domain length, radius of the Earth, and density of seawater, respectively.

| | |
|---|---|
| $A$ | $2 \times 10^3$ m$^2$s$^{-1}$ |
| $\theta_0$ | $40^\circ$ |
| $\omega$ | $7.2526 \times 10^{-5}$ s$^{-1}$ |
| $H$ | $1 \times 10^3$ m |
| $L$ | $1 \times 10^6$ m |
| $r_e$ | $6.3781 \times 10^6$ m |
| $\rho$ | $1.027 \times 10^3$ kg/m$^3$ |

Using the approximation for $\beta$ in (73), the parameter values in Table 8, and the value $\tau_0 = 0.06\ kg\ m^{-1}s^{-2}$ from [58] yields the following approximation for the characteristic velocity scale in (72):

$$U \approx 1.054 \times 10^{-2} m s^{-1}. \tag{74}$$

Using (73), (74) and the value for $L$ given in Table 8, definition (8) yields the following value for the Rossby number:

$$Ro = 6.051 \times 10^{-4}. \tag{75}$$

Using (74) and the values for $L$ and $A$ given in Table 8, definition (9) yields the following value for the Reynolds number:

$$Re = 5.27. \tag{76}$$

Since there is no exact solution available for our computational setting, we used a high-resolution numerical simulation as benchmark (i.e., "truth" solution) for all our numerical experiments. This high-resolution numerical simulation used a mesh with $h = \frac{1}{640}$ and 955302 DoFs, which was the highest resolution achievable with the available computational resources.

Fig. 6 presents a plot of the streamfunction approximation obtained by using the Argyris element on the fine mesh (i.e., with $h = \frac{1}{640}$ and 955302 DoFs) with the parameters $Ro = 6.051 \times 10^{-4}$ and $Re = 5.27$ given in (75) and (76), respectively. The streamfunction plot in Fig. 6 is qualitatively similar to the plot in Fig. 2.22 in [16]. We note that the islands considered in [16] were not connected to the nearest land mass. This is likely the main reason for the differences between the plots in Fig. 2.22 in [16] and Fig. 6 in our report. We plan to investigate the more realistic setting used in [16] in a future study.

Table 9 presents the errors $e_0, e_1, e_2$ for various meshsizes. The error converges to zero in all three norms, as expected. We note, however, that the errors in Table 9 do not follow the theoretical rates of convergence predicted by estimates (54)–(56) in Theorem 4. Specifically, the rates of convergence in Table 9 are significantly lower than the theoretical rates of convergence in Theorem 4. This behavior, however, is standard for higher-order numerical methods like that used in this report. Indeed, for uniform meshes, it is well-known that an $r^\alpha$ singularity with $0 < \alpha < 1$ yields at most $\mathcal{O}(h^\alpha)$ convergence rates for $C^0$ elements (see, e.g., [59–62]). Since we do not know the exact solution for the Mediterranean Sea example considered in our setting, we do not know whether the exact solution possesses an $r^\alpha$ singularity with $0 < \alpha < 1$. We emphasize, however, that the computational domain in Figs. 5 and 6 does possess reentrant corners that often yield this type of singularity [27–29,60–62]. A standard approach used in recovering the optimal rates of convergence for high-order $C^0$ elements is the use of graded mesh refinement (e.g., radical meshes) (see, e.g., [27–29,60–62] and the references therein). In [29], for a second order elliptic boundary value problem, a radical mesh was used to recover the optimal rates of convergence for the Argyris element, which is the $C^1$ element used in this report. We plan to extend the approach in [29] to our QGE setting in a future study. We also note that a similar decrease in the numerical solution accuracy was observed in [10] for the FE discretization of the steady linear QGE with a low-order $C^0$ piecewise linear element. Numerical inaccuracies were reported for rectangular domains with boundary layers (see Test 2 and Test 3 in [10]) and for domains with reentrant corners (see the L-shaped domain in Test 4

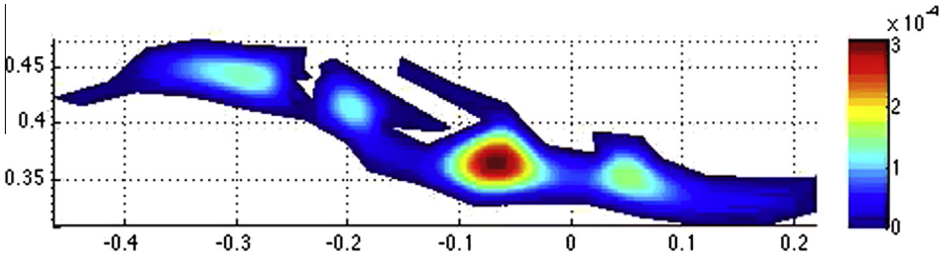


**Fig. 6.** QGE (10), Test 7: Streamfunction, $\psi^h$, on a Mediterranean Sea mesh with $h = \frac{1}{640}$ and 955302 DoFs.

**Table 9**
QGE (10), Test 7: The errors $e_0, e_1, e_2$ for various meshsizes $h$.

| $h$ | *DoFs* | $e_0$ | $L^2$ order | $e_1$ | $H^1$ order | $e_2$ | $H^2$ order |
|---|---|---|---|---|---|---|---|
| 1/2 | 1122 | $2.08 \times 10^{-6}$ | – | $1.95 \times 10^{-4}$ | – | $4.50 \times 10^{-2}$ | – |
| 1/40 | 4092 | $8.00 \times 10^{-7}$ | 1.38 | $6.68 \times 10^{-5}$ | 1.54 | $2.50 \times 10^{-2}$ | 0.850 |
| 1/80 | 15594 | $2.91 \times 10^{-7}$ | 1.46 | $2.47 \times 10^{-5}$ | 1.43 | $1.49 \times 10^{-2}$ | 0.741 |
| 1/160 | 60846 | $1.04 \times 10^{-7}$ | 1.49 | $9.05 \times 10^{-6}$ | 1.45 | $8.67 \times 10^{-3}$ | 0.785 |
| 1/320 | 240342 | $3.10 \times 10^{-8}$ | 1.75 | $2.75 \times 10^{-6}$ | 1.72 | $4.35 \times 10^{-3}$ | 0.994 |

in [10]). The numerical study in [10] clearly shows that complex domains (with reentrant corners) can yield a decrease in solution accuracy even for low-order $C^0$ elements, although this decrease is not as significant as that for high-order $C^1$ elements. A mesh refinement strategy was used in [10] to obtain optimal convergence rates for the low-order FE discretization. As already noted, we plan to use a similar mesh refinement approach in our QGE setting in a future study.

## 6. Conclusions

This paper introduced a conforming FE discretization of the streamfunction formulation of the stationary one-layer QGE based on the Argyris element. For this FE discretization, we proved optimal error estimates in the $H^2, H^1$ and $L^2$ norms. A careful numerical investigation of the FE discretization was also performed. To this end, the QGE as well as the linear Stommel and Stommel–Munk models (two standard simplified settings used in the geophysical fluid dynamics literature [10,9,4]) were used in the numerical tests. Based on the numerical results from the seven tests considered, we drew the following two conclusions: (i) our numerical results are close to those used in the published literature [10,9,4]; and (ii) the convergence rates of the numerical approximations do indeed follow the theoretical error estimates in Theorems 3 and 4. The convergence rates followed exactly the theoretical ones in the test problems where the exact solution did not display a thin boundary layer, but where somewhat lower than expected in those tests that displayed a thin western boundary layer, as expected. Furthermore, for the Mediterranean Sea test case the convergence rates were significantly lower than the theoretical convergence rates. We attribute this behavior, which is standard for high-order numerical methods, to the loss of regularity of the exact solution due to the reentrant corners displayed by the computational domain.

This paper laid rigorous mathematical foundations and provided numerical validation for the conforming FE discretization of the streamfunction formulation of the QGE. We emphasize, however, that other formulations (e.g., the streamfunction–vorticity formulation), other types of FEs (e.g., nonconforming and lower-order), and other numerical methods (e.g., finite difference, finite volume and spectral methods) can and should be used in the numerical discretization of the QGE. Just as for the NSE, although each choice has well-documented advantages and disadvantages, they all contribute to a better understanding of the underlying problem.

We plan to extend this study in several directions. First, we will treat the case of multiply connected domains [9,19,35,36] in order to allow the numerical investigation of more realistic computational domains (e.g., islands in the Mediterranean Sea and in the North Atlantic). Second, we will extend to the QGE setting the mesh refinement approach in [29] to recover optimal error estimates for the Argyris element on domains with reentrant corners, such as the Mediterranean Sea and the North Atlantic. We note that a similar mesh refinement strategy was successfully used in [10] to alleviate the numerical inaccuracies of a low-order $C^0$ FE discretization of the linearized QGE in domains with reentrant corners. Finally, we will consider the time-dependent QGE and the two-layer QGE (which will allow the study of stratification effects).

## Acknowledgement

The first and second authors greatly appreciate the support of the National Science Foundation via grant DMS-1025314 under the Collaboration in Mathematical Geosciences (CMG) initiative. The third author was supported by the institute for Mathematics and its Applications with funds provided by the National Science Foundation. We thank the anonymous reviewers for their constructive comments, which helped improve the manuscript.

## References

[1] B. Cushman-Roisin, J.M. Beckers, Introduction to Geophysical Fluid Dynamics: Physical and Numerical Aspects, Academic Press, 2011.
[2] A. Majda, X. Wang, Nonlinear Dynamics and Statistical Theories for Basic Geophysical Flows, Cambridge University Press, 2006.
[3] J. Pedlosky, Geophysical Fluid Dynamics, second ed., Springer-Verlag, 1992.
[4] G.K. Vallis, Atmosphere and Ocean Fluid Dynamics: Fundamentals and Large-scale Circulation, Cambridge University Press, 2006.
[5] H.E. Dijkstra, Nonlinear Physical Oceanography: A Dynamical Systems Approach to the Large Scale Ocean Circulation and El Nino, vol. 28, Springer-Verlag, 2005.
[6] O. San, A.E. Staples, Z. Wang, T. Iliescu, Approximate deconvolution large eddy simulation of a barotropic ocean circulation model, Ocean Model. 40 (2011) 120–132.
[7] T.D. Ringler, J. Thuburn, J.B. Klemp, W.C. Skamarock, A unified approach to energy conservation and potential vorticity dynamics for arbitrarily-structured C-grids, J. Comput. Phys. 229 (2010) 3065–3090.
[8] Q. Chen, T.D. Ringler, M. Gunzburger, A co-volume scheme for the rotating shallow water equations on conforming non-orthogonal grids, J. Comput. Phys. 240 (2013) 174–197.
[9] P.G. Myers, A.J. Weaver, A diagnostic barotropic finite-element ocean circulation model, J. Atmos. Oceanic Technol. 12 (1995) 511–526.
[10] J.M. Cascon, G.C. Garcia, R. Rodriguez, A priori and a posteriori error analysis for a large-scale ocean circulation finite element model, Comput. Methods Appl. Mech. Engrg. 192 (2003) 5305–5327.
[11] G. Fix, Finite element models for ocean circulation problems, SIAM J. Appl. Math. 29 (1975) 371–387.
[12] C. LeProvost, C. Bernier, E. Blayo, A comparison of two numerical methods for integrating a quasi-geostrophic multilayer model of ocean circulations: finite element and finite difference methods, J. Comput. Phys. 110 (1994) 341–359.
[13] W.N.R. Stevens, Finite element, stream function–vorticity solution of steady laminar natural convection, Int. J. Numer. Methods Fluids 2 (1982) 349–366.
[14] T.T. Medjo, Mixed formulation of the two-layer quasi-geostrophic equations of the ocean, Numer. Methods PDEs 15 (1999) 489–502.
[15] T.T. Medjo, Numerical simulations of a two-layer quasi-geostrophic equation of the ocean, SIAM J. Numer. Anal. 37 (2000) 2005–2022.
[16] P. Galán del Sastre, Estudio numérico del atractor en ecuaciones de Navier-Stokes aplicadas a modelos de circulación del océano, Ph.D. thesis, Universidad Complutense de Madrid, 2004.
[17] R. Bermejo, P. Galán del Sastre, Long-term behavior of the wind stress circulation of a numerical North Atlantic Ocean circulation model, in: European Congress on Computational Methods in Applied Sciences and Engineering, ECCOMAS, pp. 1–21.
[18] P. Galán del Sastre, R. Bermejo, Error estimates of proper orthogonal decomposition eigenvectors and Galerkin projection for a general dynamical system arising in fluid models, Numer. Math. 110 (2008) 49–81.
[19] M.D. Gunzburger, Finite Element Methods for Viscous Incompressible Flows, Computer Science and Scientific Computing, Academic Press Inc, 1989.
[20] V. Girault, P.A. Raviart, Finite Element Approximation of The Navier–Stokes Equations, Lecture Notes in Mathematics, vol. 749, Springer-Verlag, 1979.
[21] V. Girault, P.A. Raviart, Finite Element Methods for Navier–Stokes Equations: Theory and Algorithms, Computational Mathematics, vol. 5, Springer-Verlag, 1979.

[22] R. Kupferman, A central-difference scheme for a pure stream function formulation of incompressible viscous flow, SIAM J. Sci. Comput. 23 (2001) 1–18.
[23] J.-G. Liu, J. Liu, R.L. Pego, Stability and convergence of efficient Navier–Stokes solvers via a commutator estimate, Commun. Pure Appl. Math. 60 (2007) 1443–1487.
[24] J.-G. Liu, J. Liu, R.L. Pego, Stable and accurate pressure approximation for unsteady incompressible viscous flow, J. Comput. Phys. 229 (2010) 3428–3453.
[25] M. Ben-Artzi, J.-P. Croisille, D. Fishelov, S. Trachtenberg, A pure-compact scheme for the streamfunction formulation of Navier–Stokes equations, J. Comput. Phys. 205 (2005) 640–664.
[26] M. Ben-Artzi, J.-P. Croisille, D. Fishelov, Convergence of a compact scheme for the pure streamfunction formulation of the unsteady Navier–Stokes system, SIAM J. Numer. Anal. 44 (2006) 1997–2024.
[27] A.M. Soane, Variational problems in weighted Sobolev spaces with applications to computational fluid dynamics, Ph.D. thesis, University of Maryland at Baltimore County, 2008.
[28] A.M. Soane, R. Rostamian, Variational problems in weighted Sobolev spaces on non-smooth domains, Quart. Appl. Math. 68 (2010) 439–458.
[29] A.M. Soane, M. Suri, R. Rostamian, The optimal convergence rate of a $C^1$ finite element method for non-smooth domains, J. Comput. Appl. Math. 233 (2010) 2711–2723.
[30] D. Fishelov, M. Ben-Artzi, J.-P. Croisille, Recent developments in the pure streamfunction formulation of the Navier–Stokes system, J. Sci. Comput. 45 (2010) 238–258.
[31] C.A.M. Silva, E.N. Macêdo, J.N.N. Quaresma, L.M. Pereira, R.M. Cotta, Integral transform solution of the Navier–Stokes equations in full cylindrical regions with streamfunction formulation, Int. J. Numer. Methods Biomed. Engng. 26 (2010) 1417–1434.
[32] Z.F. Tian, P.X. Yu, An efficient compact difference scheme for solving the streamfunction formulation of the incompressible Navier–Stokes equations, J. Comput. Phys. 230 (2011) 6404–6419.
[33] F. Fairag, A two-level finite-element discretization of the stream function form of the Navier–Stokes equations, Comput. Math. Appl. 36 (1998) 117–127.
[34] F. Fairag, Numerical computations of viscous, incompressible flow problems using a two-level finite element method, SIAM J. Sci. Comput. 24 (2003) 1919–1929.
[35] M.D. Gunzburger, J.S. Peterson, Finite-element methods for the streamfunction-vorticity equations: boundary-condition treatments and multiply connected domains, SIAM J. Sci. Stat. Comput. 9 (1988) 650–668.
[36] M.D. Gunzburger, J.S. Peterson, On finite element approximations of the streamfunction-vorticity and velocity–vorticity equations, Int. J. Numer. Methods Fluids 8 (1988) 1229–1240.
[37] G. Fix, M. Gunzburger, R. Nicolaides, J. Peterson, Mixed finite element approximations for the biharmonic equations, in: J.T. Oden (Ed.), Proc. 5th Int. Symposium Finite Elements and Flow Problems, University of Texas, Austin, 1984.
[38] M. Ghil, M.D. Chekroun, E. Simonnet, Climate dynamics and fluid mechanics: natural variability and related uncertainties, Phys. D 237 (2008) 2111–2126.
[39] A. Majda, Introduction to PDEs and Waves for the Atmosphere and Ocean, American Mathematical Society, New York, 2003.
[40] J. McWilliams, Fundamentals of Geophysical Fluid Dynamics, Cambridge University Press, 2006.
[41] J. Wang, G.K. Vallis, Emergence of Fofonoff states in inviscid and viscous ocean circulation models, J. Mar. Res. 52 (1994) 83–127.
[42] R.J. Greatbatch, B.T. Nadiga, Four-gyre circulation in a barotropic model with double-gyre wind forcing, J. Phys. Oceanogr. 30 (2000) 1461–1471.
[43] D.B. Haidvogel, A.R. Robinson, E.E. Schulman, The accuracy, efficiency, and stability of three numerical models with application to open ocean problems, J. Comput. Phys. 34 (1980) 1–53.
[44] P.F. Cummins, Inertial gyres in decaying and forced geostrophic turbulence, J. Mar. Res. 50 (1992) 545–566.
[45] M.E. Cayco, R.A. Nicolaides, Finite element technique for optimal pressure recovery from stream function formulation of viscous flows, Math. Comput. 46 (1986).
[46] W.J. Layton, Introduction to The Numerical Analysis of Incompressible Viscous Flows, Society for Industrial and Applied Mathematics 6 (2008).
[47] V. Barcilon, P. Constantin, E.S. Titi, Existence of solutions to the Stommel–Charney model of the Gulf Stream, SIAM J. Math. Anal. 19 (1988) 1355–1364.
[48] G. Wolansky, Existence, uniqueness, and stability of stationary barotropic flow with forcing and dissipation, Commun. Pure Appl. Math. 41 (1988) 19–46.
[49] R. Temam, Navier–Stokes Equations: Theory and Numerical Analysis, American Mathematical Society 2 (2001).
[50] P. Ciarlet, The Finite Element Method for Elliptic Problems, North-Holland, 1978.
[51] C. Johnson, Numerical Solution of Partial Differential Equations by the Finite Element Method, vol. 32, Cambridge university press, New York, 1987.
[52] D. Braess, Finite elements: Theory, Fast Solvers, and Applications in Solid Mechanics, Cambridge University Press, 2001.
[53] V. Dominguez, F.J. Sayas, A simple Matlab implementation of Argyris element, Technical Report, 25, Universidad de Zaragoza, 2006.
[54] G. Galdi, An Introduction to The Mathematical Theory of The Navier-Stokes Equations. Vol. I, Springer Tracts in Natural Philosophy, vol. 38, Springer-Verlag, New York, 1994.
[55] H. Blum, R. Rannacher, R. Leis, On the boundary value problem of the biharmonic operator on domains with angular corners, Math. Methods Appl. Sci. 2 (1980) 556–581.
[56] C. Geuzaine, J.-F. Remacle, Gmsh: a 3-D finite element mesh generator with built-in pre-and post-processing facilities, Int. J. Numer. Methods Engrg. 79 (2009) 1309–1331.
[57] K. Bryan, A numerical investigation of a nonlinear model of a wind-driven ocean, J. Atmos. Sci. 20 (1963) 594–606.
[58] S. Hellerman, M. Rosenstein, Normal monthly wind stress over the world ocean with error estimates, J. Phys. Oceanogr. 13 (1983) 1093–1104.
[59] L.B. Wahlbin, On the sharpness of certain local estimates for $H_0^1$ projections into finite element spaces: influence of a re-entrant corner, Math. Comput. 42 (1984) 1–8.
[60] A. Ern, J.-L. Guermond, Theory and Practice of Finite Elements, Applied Mathematical Sciences, vol. 159, Springer-Verlag, New York, 2004.
[61] H.C. Elman, D.J. Silvester, A.J. Wathen, Finite Elements and Fast Iterative Solvers: With Applications in Incompressible Fluid ynamics, Oxford University Press, 2005.
[62] C. Johnson, Numerical Solution of Partial Differential Equations by the Finite Element Method, Dover Publications, 2012.